

Analysis of Ferroelectric Negative Capacitance-Hybrid MEMS Actuator Using Energy-Displacement Landscape

Raghuram Tattamangalam Raman, Jeffin Shibu, Revathy Padmanabhan and Arvind Ajoy

Abstract—We propose an energy-based framework to analyze the statics and dynamics of a ferroelectric negative capacitance-hybrid Microelectromechanical System (MEMS) actuator. A mapping function that relates the charge on the ferroelectric to displacement of the movable electrode, is used to obtain the Hamiltonian of the hybrid actuator in terms of displacement. We then use graphical energy-displacement and phase portrait plots to analyze static pull-in, dynamic pull-in and pull-out phenomena of the hybrid actuator. Using these, we illustrate the low-voltage operation of the hybrid actuator to static and step inputs, as compared to the standalone MEMS actuator. The results obtained are in agreement with the analytical predictions and numerical simulations. The proposed framework enables straightforward inclusion of adhesion between the contacting surfaces, modeled using van der Waals force. We show that the pull-in voltage is not affected, while the pull-out voltage is reduced due to adhesion. The proposed framework provides a physics-based tool to design and analyze negative capacitance based low-voltage MEMS actuators.

Index Terms—Microelectromechanical System (MEMS), Electrostatic MEMS Actuator, Ferroelectric Negative Capacitance, Energy-Displacement Landscape, Phase-portrait.

I. INTRODUCTION

ELECTROSTATIC MEMS (Microelectromechanical System) actuators are of great interest in modern electronic applications like Radio Frequency (RF) MEMS switches and digital micromirror devices [1]–[3]. While these devices are energy efficient, they demand high operating voltages [3]. Ultra-scaled MEMS devices can operate at low-voltages, but are challenging to fabricate reliably due to effects such as stiction [4]. Masuduzzaman and Alam [5] proposed a novel approach to reduce the operating voltage of a MEMS device without scaling its air-gap. Their *hybrid* MEMS actuator consists of a ferroelectric capacitor, exhibiting negative capacitance, connected in series with the MEMS actuator. This idea is similar to the development of Negative Capacitance-Field Effect Transistors (NC-FETs), proposed originally in Ref. [6]. Readers are directed to Refs. [7], [8] for a review of NC-FETs. Low-voltage operation is predicted to arise due to

the internal voltage amplification when a negative capacitance is connected in series with a positive capacitance. Different signatures of negative capacitance in ferroelectrics have been experimentally reported – for example, a charge-voltage curve with negative slope [9], [10], an enhanced total capacitance [11], and steady state charge boost [12] in a ferroelectric-dielectric heterostructure.

No experimental realizations of the hybrid actuator have been reported so far. Many authors have analyzed the performance of these devices through analytical and numerical techniques. The ferroelectric capacitor is governed by the nonlinear Landau-Khalatnikov equation [5], which relates the voltage across the ferroelectric to its charge. The MEMS actuator, on the other hand, is governed by a nonlinear differential equation [13], expressed in terms of displacement of the movable electrode. It is convenient to describe both the ferroelectric and the MEMS actuator in terms of a common entity. For instance, the response of the hybrid actuator to slowly varying (quasi-static) inputs was analytically studied in Refs. [5], [14] using charge as the common variable. They solve the algebraic equations that describe the balance between the electrostatic attraction and spring restoring forces at equilibrium. Our earlier work [15] analyzes both the static and dynamic response of standalone MEMS actuators based on their energy-charge landscape. This technique can, in principle, be extended to analyze the hybrid actuator as well.

However, for many applications, displacement is a more natural coordinate used to analyze MEMS actuators [13]. Analysis based on displacement is convenient to include effects such as adhesion [16]–[18] and a non-linear spring [19], that are directly described in terms of displacement. We had developed [20] a numerical model to analyze both the statics and dynamics of the hybrid actuator, based on displacement. The numerical model solves the nonlinear, coupled, differential equations using the inbuilt solvers of a circuit simulator. The numerical approach, though, provides very limited physical insight into the response of the hybrid actuator.

In this work, we develop a physics-based graphical framework, using displacement as the dynamical variable, that facilitates a systematic analysis of the statics and dynamics of the hybrid actuator. We employ a coordinate transformation from the charge to the displacement of the movable electrode, in order to describe the ferroelectric in terms of displacement. This allows us to express the Hamiltonian (energy) of the

R. Tattamangalam Raman, J. Shibu, R. Padmanabhan and A. Ajoy are with Electrical Engineering, Indian Institute of Technology Palakkad, Palakkad, India. e-mail: 121704004@smail.iitpkd.ac.in; 121801055@smail.iitpkd.ac.in; revathyp@iitpkd.ac.in; arvinda-joy@iitpkd.ac.in

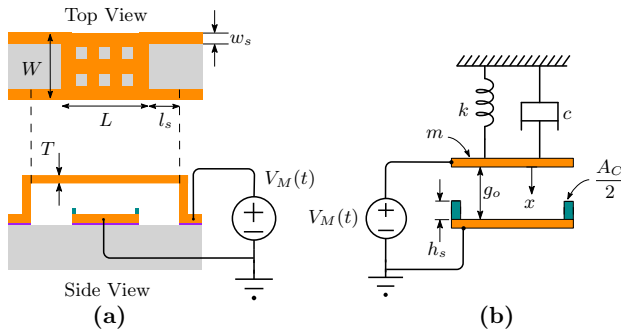


Fig. 1. (a) Schematic representation of the standalone clamped-clamped MEMS actuator. (b) Equivalent 1-DOF model of the MEMS actuator.

hybrid MEMS actuator in terms of displacement. We then use graphical energy-displacement and phase portrait (velocity vs. displacement) plots to investigate static pull-in, dynamic pull-in and pull-out phenomena of the hybrid MEMS actuator.

The usefulness of describing the Hamiltonian in terms of displacement is illustrated by studying the effect of adhesion in the hybrid actuator. Adhesion plays a major role when the top electrode comes in contact with the bottom surface. We include the effect of adhesion between contacting surfaces, by adding a term corresponding to the van der Waals force [16]–[18] into the Hamiltonian of the system. We show that adhesion reduces the pull-out voltage but does not affect the pull-in voltage. We demonstrate how the actuator can be redesigned so that the reduction in pull-out voltage (due to adhesion) can be compensated. We show that this redesign causes an increase in the pull-in voltage; nevertheless, the new pull-in voltage is predicted to still be considerably lower than the pull-in voltage of the standalone MEMS actuator. Since the proposed energy framework uses only graphical plots for the analysis, this serves as a quick design and analysis tool to predict the pull-in and pull-out behaviour of the hybrid actuator.

This article is organized as follows. Section II reviews the operation of the standalone and hybrid MEMS actuators. Section III presents the Hamiltonian of the hybrid actuator using the displacement of the movable electrode as the dynamical variable. Section IV discusses our design of the hybrid actuator. The static pull-in, dynamic pull-in and pull-out of the hybrid actuator are analyzed in Section V. Section VI investigates the effect of adhesion. Finally, Section VII presents our conclusions.

II. REVIEW OF STANDALONE AND HYBRID MEMS ACTUATORS

We consider a standalone electrostatic MEMS actuator as a clamped-clamped beam with fixed-fixed flexure, as shown in Fig. 1(a). Based on Refs. [3], [21], the values of the MEMS actuator parameters are listed in Table I and are fairly typical for MEMS actuators. These references also detail the fabrication steps used to realize such MEMS actuators. The actuator is modeled using a single degree of freedom (1-DOF), parallel plate arrangement consisting of a pair of electrodes separated by an air-gap g_o , as shown in Fig. 1(b). It is excited by an input voltage $V_M(t)$, where t denotes time. The top

TABLE I
PARAMETERS OF THE HYBRID MEMS ACTUATOR USED IN THIS WORK

Parameter	Value
Beam material	Gold (Au) [21]
Length of the beam, L	$140 \mu\text{m}$
Width of the beam, W	$120 \mu\text{m}$
Actuation area, A_M	$1.44 \times 10^{-8} \text{m}^2$
Young's modulus, E	78 GPa
Density, D	19280kg/m^3
Mass, $m = 0.35 \times D \times \text{volume}$	$5.6 \times 10^{-11} \text{kg}$ [3]
Width of the support, w_S	$20 \mu\text{m}$
Length of the support, l_S	$80 \mu\text{m}$
Thickness, T	$0.5 \mu\text{m}$
Spring constant, $k = 4Ew_s(\frac{T}{l_s})^3$	1.52N/m [3]
Initial air-gap, g_o	$2 \mu\text{m}$
Stopper height, h_s	$0.15 \mu\text{m}$
Area of contact, A_C	$16 \mu\text{m}^2$ [17]
Permittivity of free space, ϵ_o	$8.854 \times 10^{-12} \text{F/m}$
Ferroelectric material	HfO ₂ [22]
α_F	$-2.88 \times 10^9 \text{m/F}$
β_F	$3.56 \times 10^{11} \text{m}^5/\text{F/C}^2$
γ_F	$0 \text{m}^9/\text{F/C}^4$
Ferroelectric thickness, t_F	45.24nm
Ferroelectric area, A_F	$9.87 \mu\text{m}^2$

electrode is movable and the bottom electrode is fixed. The stiffness of the beam, the inertia elements and the damping mechanisms of the actuator are effectively represented by a spring-mass-damper with spring constant k , mass m , and damping coefficient c . We assume that the displacement of the top electrode, denoted by a dynamical variable x , is limited by a pair of stoppers, as shown in Fig. 1(b). These stoppers (with height h_s) are made of an insulating material and hence, prevent electrical short between the top and bottom electrodes [23], [24]. The top electrode comes in contact with the stopper over an area A_C . We neglect damping in our analysis. The effect of surface forces is neglected initially and included later in Section VI.

The transient response of the MEMS actuator depends on the nature of the input voltage. The input voltage is considered to be *slow* if its rise time, t_{inp} , is significantly greater than the system rise time, t_{sys} of the MEMS actuator. Empirically, $t_{sys} = 0.35/f_0$, where the resonant frequency $f_0 = \frac{1}{2\pi} \sqrt{k/m}$ [25]. Thus, when $t_{inp} \gg t_{sys}$, the actuator remains in quasi-static equilibrium. However, beyond a certain voltage, called the static pull-in voltage V_{SPI} , the movable electrode snaps down on to the fixed electrode. This condition is called static

TABLE II
PULL-IN AND PULL-OUT OF A STANDALONE MEMS ACTUATOR. VALUES CORRESPOND TO PARAMETERS LISTED IN TABLE I.

Parameter	Expression [13]	Value
Static pull-in voltage, V_{SPI}	$\sqrt{8kg_o^3/27\epsilon_o A_M}$	5.32 V
Travel range, X_{SPI}	$g_o/3$	$0.67 \mu\text{m}$
Dynamic pull-in voltage, V_{DPI}	$\sqrt{kg_o^3/4\epsilon_o A_M}$	4.88 V
Dynamic pull-in displacement, X_{DPI}	$g_o/2$	$1 \mu\text{m}$
Pull-out voltage, V_{PO}	$\sqrt{\frac{2k}{\epsilon_o} \frac{h_s^2}{A_M} (g_o - h_s)}$	1 V
System rise time, t_{sys}	$0.35 \times 2\pi \sqrt{m/k}$	$13.28 \mu\text{s}$

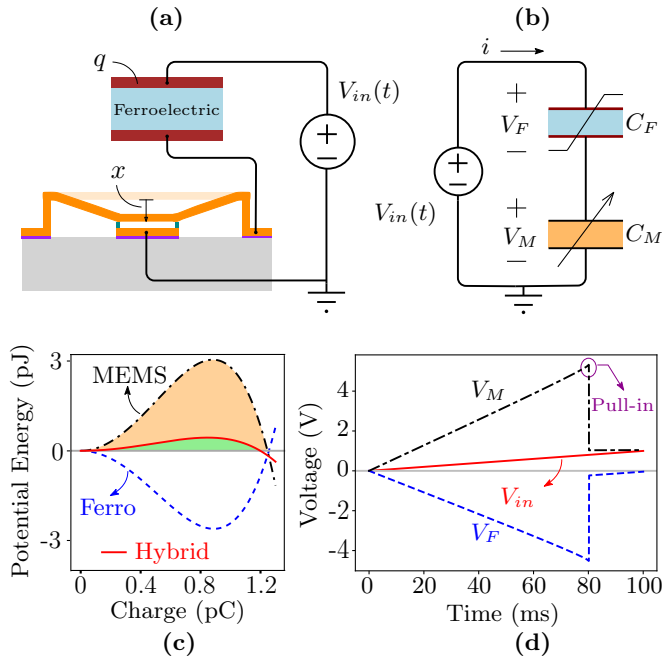


Fig. 2. (a) Hybrid actuator formed by series connection of ferroelectric capacitor C_F with the MEMS actuator. (b) Equivalent circuit representation. C_M represents the variable capacitance provided by the MEMS actuator. (c) Potential energy-charge landscape plotted for $V_{in} = 0$ V, depicting a lowered energy barrier (shaded green) in the hybrid actuator as compared to the MEMS actuator (shaded orange). (d) Voltages plotted as a function of time. The hybrid actuator operates at a lower voltage due to the voltage amplification ($V_M > V_{in}$) caused by the ferroelectric negative capacitance.

pull-in [13]. Consequently, the maximum distance travelled by the movable electrode, before it snaps down, is called the travel range X_{SPI} . On the other hand, for a step input (with $t_{act} \ll t_{sys}$), the actuator is driven away from equilibrium. In the absence of damping, the response of the actuator is oscillatory, for voltages less than V_{DPI} , called the dynamic pull-in voltage. The maximum value of this oscillatory displacement of the electrode is referred to as the dynamic pull-in displacement, X_{DPI} . For any applied step voltage, greater than V_{DPI} , the movable top electrode snaps down onto the bottom electrode. This condition is called dynamic pull-in [13]. After achieving pull-in (static or dynamic), as the input voltage is reduced to a specific value, called the pull-out voltage V_{PO} , the pull-in condition is lost and the movable top electrode gets detached from the fixed bottom electrode. This condition is called pull-out [13]. Table II summarizes the expressions for pull-in/pull-out voltages and displacements for a standalone electrostatic MEMS beam, with zero damping. The corresponding values for the actuator described in Table I are also listed. Note that damping does not affect pull-out and static pull-in. However, with an increase in damping constant c , the dynamic pull-in voltage increases from V_{DPI} and approaches the static pull-in voltage V_{SPI} [26]. Hence the analysis presented in this work (with $c = 0$) provides an estimate of the lowest possible dynamical pull-in voltage.

The hybrid actuator is formed by connecting a ferroelectric capacitor C_F , in series with the standalone MEMS actuator, as shown in Fig. 2(a). This configuration is similar to various neg-

ative capacitance transistors reported in literature, where the ferroelectric capacitor is connected externally to the transistor [27]–[33]. The equivalent circuit representation of the hybrid actuator is shown in Fig. 2(b), wherein the MEMS actuator is depicted as a variable capacitor C_M . The low voltage operation of the hybrid MEMS actuator can be understood from the potential energy-charge landscape (plotted for $V_{in} = 0$ V in Fig. 2(c)), following Ref. [5]. The parameters assumed for the ferroelectric are listed in Table I and will be discussed later in Section IV. Note that the energy barrier is lowered in the hybrid actuator as compared to that of the standalone MEMS actuator. This observation is substantiated by numerical results shown in Fig. 2(d), based on Ref. [20]. The voltage across MEMS actuator V_M is larger than the applied input voltage V_{in} since the voltage across the ferroelectric V_F is negative. This internal voltage amplification results in a lower pull-in voltage (corresponding to a lower energy barrier) in the hybrid MEMS actuator as compared to the standalone MEMS actuator.

III. HAMILTONIAN OF THE HYBRID ACTUATOR

The Hamiltonian (total energy) H_M of the standalone electrostatic MEMS actuator (Fig. 1), is given by [15]

$$H_M(x, \dot{x}, t) = \underbrace{\frac{1}{2} m \dot{x}^2}_{\text{Kinetic energy}} + \underbrace{\frac{1}{2} k x^2 - \frac{1}{2} \frac{\epsilon_o A_M V_M^2(t)}{(g_o - x)}}_{\text{Potential energy}} \quad (1)$$

where $\dot{x} = \frac{dx}{dt}$ represents the velocity.

We assume the ferroelectric capacitor to behave as a single homogeneous domain. In the case where the ferroelectric material is inhomogeneous, the single domain assumption describes an averaged response, using an effective value of the ferroelectric coefficients [34]. Indeed, literature ([9], [27], [30], [34]–[37]) reports the use of the single domain assumption to describe experimental results with different ferroelectrics for thicknesses upto ~ 100 nm. With the single domain assumption, the Landau-Khalatnikov (LK) equation [5], [6], [9] relates the voltage across the ferroelectric capacitor V_F to the charge q (where $q = \int i dt$) as

$$V_F = -\alpha q + \beta q^3 + \gamma q^5 \quad (2)$$

$$\alpha = -\frac{\alpha_F t_F}{A_F}, \beta = \frac{\beta_F t_F}{A_F^3}, \gamma = \frac{\gamma_F t_F}{A_F^5} \quad (3)$$

where α_F , β_F and γ_F are ferroelectric anisotropy coefficients, t_F and A_F are the thickness and area of the ferroelectric respectively. The energy associated with the ferroelectric capacitor is given by

$$U_F(q) = -\frac{1}{2} \alpha q^2 + \frac{1}{4} \beta q^4 + \frac{1}{6} \gamma q^6 - V_F q \quad (4)$$

Note that the Eq. (4) is written in terms of charge q , whereas Eq. (1) is described in terms of displacement x . In this work, we use displacement of the movable electrode as the common dynamical variable to describe both the MEMS actuator and the ferroelectric capacitor. Both the ferroelectric capacitor and the MEMS actuator share the same charge q , since they are connected in series. Based on our earlier work on electrostatic MEMS actuators in Ref. [15], we relate the charge q to the

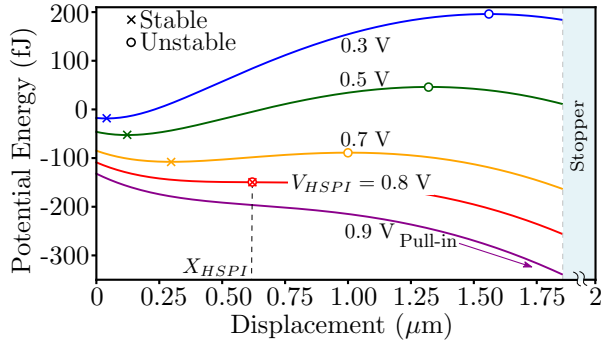


Fig. 3. Potential energy-displacement plot depicting static pull-in. Stable and unstable equilibrium displacements coincide at static pull-in voltage, $V_{HSPI} = 0.8$ V, with travel range $X_{HSPI} = 0.62$ μm .

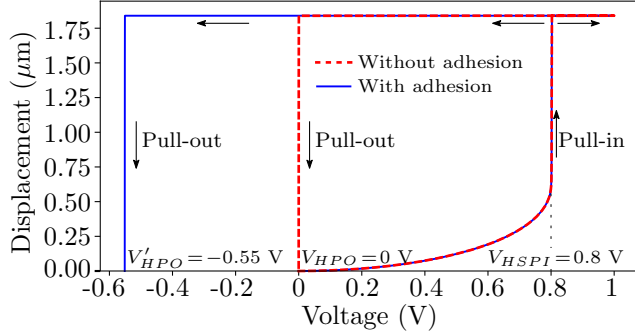


Fig. 4. Numerical simulation of the static characteristics of the hybrid actuator without (red dashed) and with (blue solid) adhesion forces. Due to adhesion, the pull-out voltage is reduced from $V_{HPO} = 0$ V to $V'_{HPO} = -0.55$ V. However, the static pull-in voltage ($= 0.8$ V) remains unchanged.

displacement x of the movable electrode, using the mapping function

$$q = \frac{\epsilon_o A_M V_M(t)}{(g_o - x)} \quad (5)$$

This mapping function is based on the charge-voltage relationship of a parallel plate capacitor. Using Eq. (2) and applying Kirchhoff's voltage law in Fig. 2, Eq. (5) can be rearranged to obtain

$$q^5 \left[\frac{\epsilon_o A_M \gamma}{g_o - x} \right] + q^3 \left[\frac{\epsilon_o A_M \beta}{g_o - x} \right] + q \left[1 - \frac{\epsilon_o A_M \alpha}{g_o - x} \right] - \frac{\epsilon_o A_M V_{in}(t)}{g_o - x} = 0 \quad (6)$$

We solve the above equation (discarding the complex roots), to obtain the charge q as a function of the applied voltage and displacement. This charge is then substituted in Eq. (2) and Eq. (4) to obtain the energy associated with the ferroelectric U_F , in terms of displacement. We can thus write the Hamiltonian of the hybrid actuator as

$$H_H(x, \dot{x}, t) = U_F(x) + H_M(x, \dot{x}, t) \quad (7)$$

where both the ferroelectric and MEMS actuator are described in terms of the displacement of the MEMS actuator. We will see later in Section VI that writing the Hamiltonian of the hybrid actuator in terms of x allows us to include the effect of adhesion in a straightforward manner.

IV. DESIGN OF THE HYBRID ACTUATOR

The effect of negative capacitance has been reported in different ferroelectric materials like $\text{PbZr}_{0.2}\text{Ti}_{0.8}\text{O}_3$ (PZT) [9], BiFeO_3 [30], Hafnium Zirconium Oxide ($\text{Hf}_x\text{Zr}_{1-x}\text{O}_2$) [10], [12], [38]–[40], P(VDF-TrFE) [41], [42] etc. In this work, we choose the parameters of Hafnium Oxide (HfO_2) as a typical ferroelectric, with coercive field $E_c = 1$ MV/cm and remanant polarization $P_r = 9$ $\mu\text{C}/\text{cm}^2$ [22]. Note that the essence of the analysis presented in this work does not depend on any particular choice of ferroelectric. The ferroelectric capacitor must be designed so as that the combination of the ferroelectric and MEMS capacitors is stable at zero applied voltage [5], [20]. Note that the standalone MEMS actuator has $V_{SPI} = 5.32$ V and $V_{PO} = 4.88$ V (see Table II). We design the ferroelectric such that the hybrid actuator has a static pull-in voltage of 0.8 V and pull-out voltage of 0 V. Following Ref. [5], [20] the static pull-in voltage of the hybrid actuator V_{HSPI} is given by

$$V_{HSPI} = r_{\alpha N} \sqrt{\frac{r_{\alpha N}}{r_{\beta N}} \cdot \frac{8 k g_o^3}{27 \epsilon_o A_M}} \quad \text{with} \quad (8a)$$

$$r_{\alpha N} = 1 - \frac{t_F A_M |\alpha_F| \epsilon_o}{g_o A_F} \quad \text{and} \quad (8b)$$

$$r_{\beta N} = 1 - \left[\frac{2 \beta_F k t_F \epsilon_o^2 A_M^2}{A_F^3} \right] \quad (8c)$$

Pull-out of the hybrid actuator at $V_{HPO} = 0$ V requires that the distance traveled by the movable electrode $(g_o - h_s) = (r_{\alpha N}/r_{\beta N}) g_o$ [5]. Using the above equations, we obtain the required thickness t_F and area A_F of the ferroelectric, as listed in Table I.

V. ANALYSIS OF THE HYBRID ACTUATOR

From the Hamiltonian $H_H(x, \dot{x}, t)$ in Eq. (7), we obtain the potential energy-displacement relation by setting $\dot{x} = 0$. The hybrid actuator is analyzed using using the potential energy-displacement and phase-portrait (velocity-displacement) plots as explained in the following sections.

A. Static Pull-in

The potential energy-displacement plot of the hybrid actuator shown in Fig. 3 explains static pull-in. For an applied voltage less than the static pull-in voltage, there are two equilibrium displacements: stable (denoted by \times) and unstable (denoted by \circ). These equilibrium displacements coincide when the input voltage equals the static pull-in voltage of the hybrid actuator, $V_{HSPI} = 0.8$ V. Correspondingly, the travel range of the hybrid actuator, $X_{HSPI} = 0.62$ μm . Beyond V_{HSPI} , the absence of any stable equilibrium displacement results in static pull-in, as depicted in Fig. 3. The results obtained using the proposed framework exactly match with the analytical predictions (see Table III) and with the numerical simulations based on Ref. [20] shown in Fig. 4. The numerical simulations use a slowly varying ramp input (with $t_{inp} = 80$ ms $\gg t_{sys}$) as shown in Fig. 2(d).

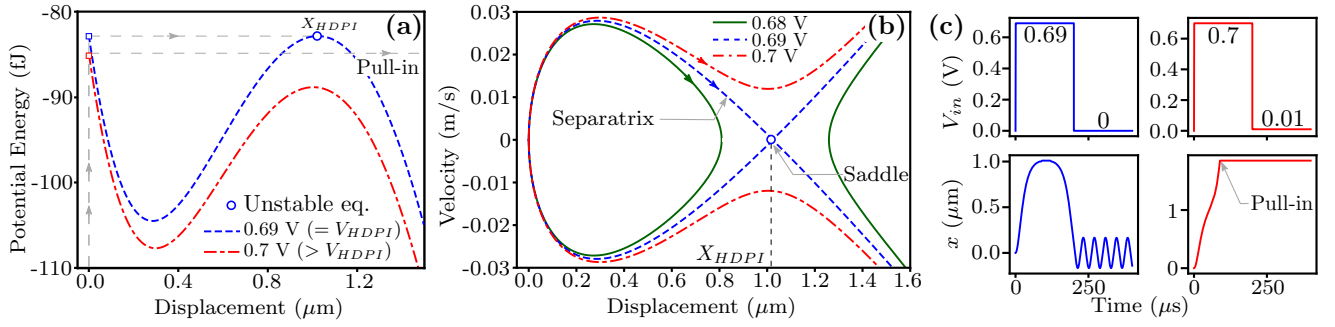


Fig. 5. Analysis of dynamic pull-in using (a) Potential energy-displacement plot. Initial energy at $x = 0$ equals the energy at the point of unstable equilibrium when the step input equals the dynamic pull-in voltage, $V_{HDPI} = 0.69$ V. Any step input greater than V_{HDPI} results in dynamic pull-in. (b) Phase-portrait. The trajectory becomes open when dynamic pull-in occurs. (c) Numerical simulation based on Ref. [20].

B. Dynamic Pull-in

Fig. 5(a) depicts dynamic pull-in in the hybrid actuator using potential energy-displacement plots. Note that the initial energy (energy at $x = 0$) equals the energy at point of the unstable equilibrium for an applied step voltage of 0.69 V. This corresponds to the dynamic pull-in voltage of the hybrid actuator, V_{HDPI} . Correspondingly, the dynamic pull-in displacement, $X_{HDPI} = 1.01$ μm , as depicted in Fig. 5(a). Any step input greater than V_{HDPI} will result in dynamic pull-in because the initial energy is greater than the energy at the point of unstable equilibrium, as illustrated in Fig. 5(a).

Dynamic pull-in can also be visualized using a phase-portrait (velocity-displacement plot). We plot the phase portrait by noting that total energy is conserved. Thus, for any step voltage V_{in} applied at $t = 0$, the total energy E_{total} can be obtained by setting $x = 0$, $\dot{x} = 0$ (corresponding to the initial conditions) in Eq. (7). We then solve the implicit algebraic equation $H_H(x, \dot{x}) = E_{total}$ to obtain \dot{x} for different values of x . The trajectory $\dot{x}(x)$ shows the evolution of the system for a specific applied step input, in the displacement-velocity phase plane. Note that time t does not appear explicitly in Eq. (7) for a step input, provided $t > 0^+$. The collection of trajectories for different applied voltages forms the phase-portrait.

See Fig. 5(b). For step input less than V_{HDPI} , the trajectory is closed, indicating an oscillatory response. The phase-portrait shows a separatrix for a step input voltage of $V_{HDPI} = 0.69$ V. The separatrix runs through a saddle point that corresponds to the dynamic pull-in displacement, $X_{HDPI} = 1.01$ μm . Any step input greater than V_{HDPI} results in dynamic pull-in, which is characterized by the open trajectory in the phase-portrait.

Results from numerical simulations for dynamic pull-in, based on Ref. [20], are shown in Fig. 5(c). They are obtained by applying a step voltage input (with $t_{inp} = 1$ ps \ll t_{sys}). The results from the graphical approach (Figs. 5(a), (b)) are in good agreement with the numerical simulations (summarized in Table III). Note that there are no analytical results for dynamic pull-in of the hybrid actuator.

C. Pull-out

The pull-out of the hybrid actuator can be visualized using the phase-portrait as shown in Fig. 6(a), (b). Note that the

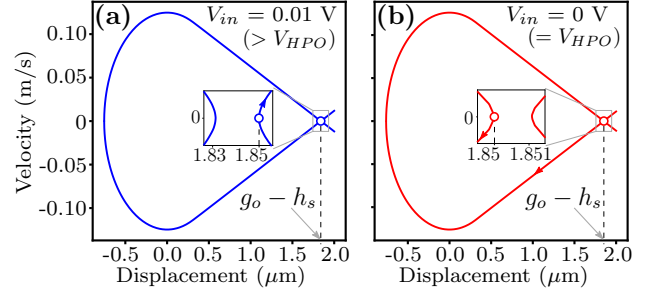


Fig. 6. Analysis of pull-out using phase-portrait. Pull-out does not occur for input greater than the pull-out voltage, V_{HPO} , as displacement $g_o - h_s$ lies on the open trajectory. Pull-out occurs when input equals $V_{HPO} = 0$ V as $g_o - h_s$ lies on the closed trajectory.

actuator has already achieved pull-in, after travelling a displacement of $x = g_o - h_s$, where g_o is the air-gap and h_s is the stopper height. Thus, for pull-out analysis, the initial displacement is at $x = g_o - h_s$, as opposed to the initial displacement of $x = 0$, for the dynamic pull-in analysis. The hybrid actuator does not pull-out when the input is reduced upto 0.01 V as the displacement $g_o - h_s$ lies on the open trajectory. However, when the input voltage is further reduced to 0 V, the displacement $g_o - h_s$ lies on the closed trajectory, indicating pull-out. The closed trajectory represents sustained oscillations, after pull-out, in the absence of damping. Hence, the pull-out voltage of the hybrid actuator $V_{HPO} = 0$ V. The estimated pull-out voltage of the hybrid actuator matches with the analytical prediction (see Table III) and with the numerical simulation shown in Fig. 4.

VI. EFFECT OF ADHESION

In this section, we analyze the pull-in and pull-out phenomena in the presence of adhesion (stiction force) between the

TABLE III
SUMMARY OF ANALYSIS OF THE HYBRID ACTUATOR

Parameter	This work	Numerical	Analytical
Static pull-in voltage, V_{HSPI}	0.8 V	0.8 V	0.8 V
Travel range, X_{HSPI}	0.62 μm	0.62 μm	0.62 μm
Dynamic pull-in voltage, V_{HDPI}	0.69 V	0.69 V	N.A.
Dynamic pull-in displacement, X_{HDPI}	1.01 μm	1.01 μm	N.A.
Pull-out voltage, V_{HPO}	0 V	0 V	0 V

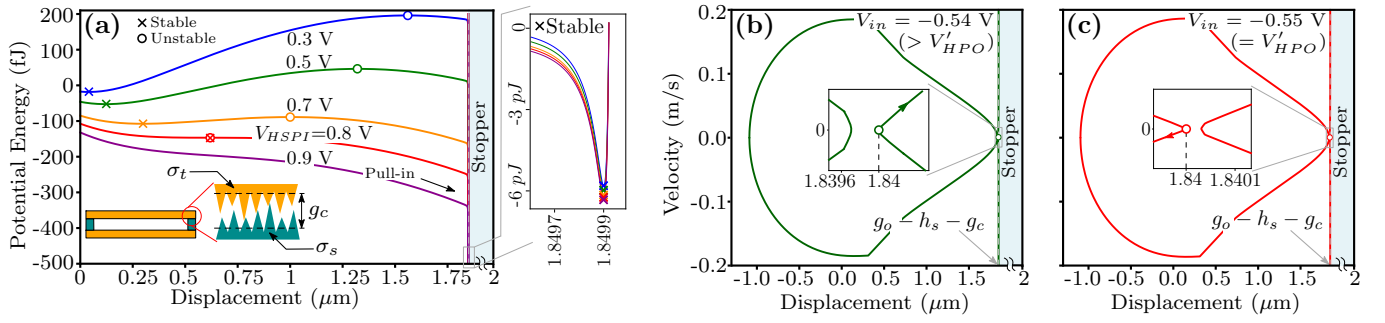


Fig. 7. Effect of adhesion in the hybrid actuator. (a) Analysis of static pull-in using energy-displacement plot. The static pull-in voltage ($= 0.8$ V) is not affected by adhesion. The plot near the contact is shown enlarged depicting the effect of adhesion. The inset in the main plot shows the effective gap at contact g_c due to surface roughness (σ_t , σ_s of the top electrode and stopper respectively), when the top electrode hits the stopper. (b), (c) Analysis of pull-out using phase-portrait. Note that the initial displacement for pull-out analysis is $g_o - h_s - g_c$ due to surface roughness. The pull-out voltage is reduced to -0.55 V as a result of adhesion.

contacting surfaces. When the beam is actuated so that the top electrode comes in contact with the stopper, adhesion plays an important role. The proposed graphical approach based on energy landscape gives physical insight into understanding the effect of adhesion. We model the adhesion between the contacting surfaces using the van der Waals force [16]–[18], [43], based on the Lennard-Jones potential and given by

$$F_{LJ}(x) = \frac{A_H A_C}{6\pi} \left(\frac{1}{\delta^3(x)} - \frac{\Lambda^6}{\delta^9(x)} \right) \quad (9)$$

where $\delta(x) = g_o - h_s - x$ is the gap between the top electrode and the stopper. A_C is the area of contact. A_H is the Hamaker constant, and Λ is the inter-atomic equilibrium distance. Eq. (9) can also be expressed as

$$F_{LJ}(x) = \frac{C_1 A_C}{\delta^3(x)} - \frac{C_2 A_C}{\delta^9(x)} \quad (10)$$

and C_1, C_2 are the attractive and repulsive constants, respectively, with typical values $C_1 = 10^{-20}$ Nm, $C_2 = 10^{-80}$ Nm⁷ [17]. The corresponding Lennard-Jones potential is given by

$$U_{LJ}(x) = \frac{-C_1 A_C}{2(g_o - h_s - x)^2} + \frac{C_2 A_C}{8(g_o - h_s - x)^8} \quad (11)$$

Since U_{LJ} is a function only of x , we can add it directly to the Hamiltonian of the hybrid actuator $H_H(x, \dot{x}, t)$. The Hamiltonian of the hybrid MEMS actuator is now modified to include the Lennard-Jones potential as

$$H_{HLJ}(x, \dot{x}, t) = H_H(x, \dot{x}, t) + U_{LJ}(x) \quad (12)$$

The effect of adhesion on the pull-in voltage is analyzed using the potential energy-displacement plot using Eq. (12) with $\dot{x} = 0$. As depicted in Fig. 7(a), the static pull-in voltage ($= 0.8$ V) is not changed due to adhesion. This is because van der Waals force is a short-range force which does not change the energy landscape in regions away from the contact.

The numerical simulation of the static characteristics in Fig. 4, based on Ref. [20], also confirms that the static pull-in voltage is unaffected due to adhesion. We have modified the simulation framework in Ref. [20] to include the effect of adhesion. Adhesion is implemented as an additional sub-circuit which models the van der Waals force (Eq. (10)). The numerical model of the standalone MEMS actuator now

estimates the acceleration a based on the following force-balance equation

$$a = \frac{F_{elec} + F_{LJ} - F_{mech}}{m} \quad (13)$$

where F_{elec} , F_{LJ} and F_{mech} are the electrostatic, van der Waals and the mechanical restoring forces, respectively. The estimated acceleration is integrated to compute the velocity \dot{x} , which is again integrated to obtain the displacement x . The integration is performed by a built-in function available in the circuit simulator. The estimated velocity and displacement are given in a feedback loop to obtain the stable solution of the electrode displacement for an applied input voltage.

Note that a deep energy well, with a stable minima very close to the stopper location ($\approx g_o - h_s$) is created due to adhesion, as shown in Fig. 7(a). When the applied voltage exceeds the pull-in voltage, pull-in occurs and the beam comes in contact with the stopper. Due to the roughness of the contact surface, there are small asperities distributed all over the contact area [see inset in Fig. 7(a)]. As a result, there exists an effective gap at contact, g_c , between the two contacting surfaces. Assuming σ_t and σ_s are the standard deviations of the thickness of the top electrode and the height of the stopper respectively, we can define $g_c = \sqrt{\sigma_t^2 + \sigma_s^2}$ [18], [44]. Therefore, after pull-in, owing to the surface roughness, the top electrode settles effectively at $g_o - h_s - g_c$. The effective gap is a random variable that varies across different fabrication runs. For the chosen dimensions of the MEMS beam, we assume $g_c = 10$ nm, based on Refs. [18], [21].

The pull-out voltage is analyzed using the phase-portrait, as shown in Fig. 7(b), (c). As explained above, after pull-in, the top electrode settles at $g_o - h_s - g_c$. Therefore, for the analysis of pull-out using the phase portrait, the initial displacement to determine the total energy is $g_o - h_s - g_c$. Contrast this with the case without adhesion and surface roughness, wherein the initial displacement for pull-out analysis is $g_o - h_s$ [see Fig. 6(a), (b)]. As shown in Fig. 7(b), (c), the displacement $g_o - h_s - g_c$ is on the closed trajectory when the input is -0.55 V. Thus, adhesion reduces the pull-out voltage from $V_{HPO} = 0$ V (without adhesion; see Table III) to $V'_{HPO} = -0.55$ V. We also confirm this reduction in the pull-out voltage using the numerical simulation of the static characteristics, as shown in

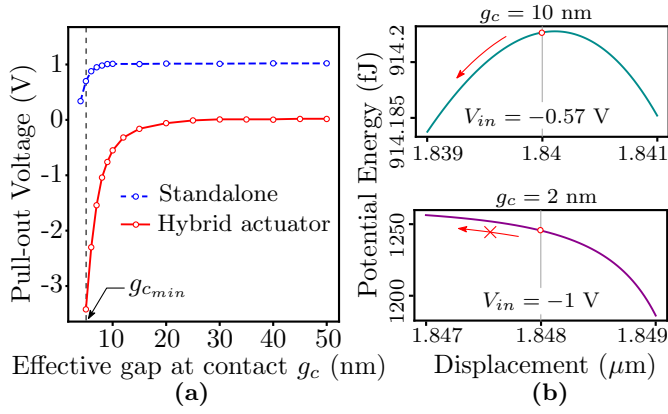


Fig. 8. (a) Variation in the pull-out voltage with respect to the change in the effective gap at contact g_c . As effective gap increases, the pull-out voltage tends towards the electrostatically estimated (without adhesion) value. (b) Energy-displacement plots for $g_c = 10$ nm and 2 nm. The presence of an energy barrier prevents pull-out for $g_c = 2$ nm ($< g_{c_{min}}$). Note that the \circ represents $(g_o - h_s - g_c)$ in both cases.

Fig. 4. Thus, the pull-in voltage is unaffected and the pull-out voltage is reduced due to adhesion.

We now study the variation in the pull-out voltage with respect to the change in the effective gap at contact (g_c), as shown in Fig. 8(a). The trend observed in the hybrid actuator is similar to the effect of adhesion on the pull-out voltage in the standalone actuator (for example, see Ref. [18]). As shown in Fig. 8(a), the pull-out voltage tends towards the electrostatically estimated value (without adhesion) with an increase in g_c . This is because adhesion force becomes negligible for higher values of g_c . As in the case of the standalone actuator, there exists a minimum effective gap at contact ($g_{c_{min}}$), in the hybrid actuator, below which pull-out does not occur in the presences of adhesion. For example, as shown in Fig. 8(b), pull-out occurs for $g_c = 10$ nm ($> g_{c_{min}}$) with $V_{in} = -0.57$ V ($< V'_{HPO}$). However, the presence of an energy barrier at $g_o - h_s - g_c = 1.848$ μ m for $g_c = 2$ nm ($< g_{c_{min}}$) prevents pull-out. Thus, the effective gap at contact g_c and hence the surface roughness plays a significant role in determining the pull-out behaviour. For instance, pull-out can be facilitated by increasing the surface roughness [45] thereby reducing stiction.

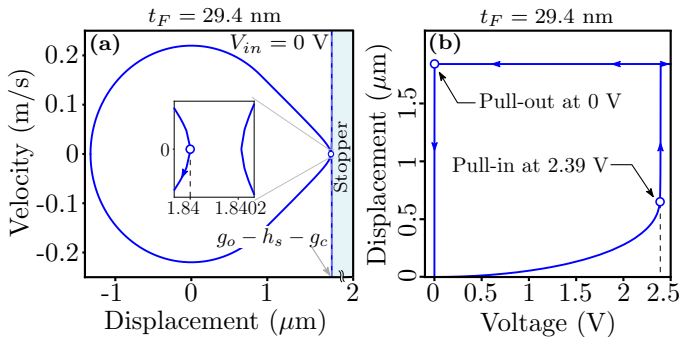


Fig. 9. (a) Phase-portrait depicting that the pull-out voltage, in the presence of adhesion, is 0 V, achieved with a reduced ferroelectric thickness of $t_F = 29.4$ nm. (b) Numerical simulation of the static characteristics of the hybrid actuator with $t_F = 29.4$ nm.

We predict that the pull-out voltage can be brought back to 0 V, even in the presence of adhesion, by tailoring the ferroelectric thickness t_F . It has been predicted that both pull-in and pull-out voltages increase with reduction in the ferroelectric thickness [20], [46]. By looking at the slope of the potential energy-displacement plot at $g_o - h_s - g_c$, we predict that a reduction of the ferroelectric thickness to 29.4 nm eliminates the barrier for pull-out at zero applied voltage, as shown in Fig. 9(a), (b). This is, however, accompanied with an increased pull-in voltage of 2.39 V. Nevertheless this increased pull-in voltage is still lower than the pull-in voltage of the standalone MEMS actuator ($=5.32$ V).

VII. CONCLUSION

To summarize, we have proposed a physics-based framework based on the energy-landscape to systematically analyze the static pull-in, dynamic pull-in and pull-out phenomena of the ferroelectric negative capacitance-hybrid MEMS actuator. Based on the proposed framework, we illustrate the low-voltage operation of the hybrid actuator for static and step inputs. The results obtained are in good agreement with analytical predictions and numerical simulations. We also include the effect of adhesion in the framework. We show that the pull-in voltage is not affected, while the pull-out voltage is reduced due to adhesion. Since the proposed framework employs graphical energy-displacement and phase-portrait plots, it serves as an easy and quick design and analysis tool. The scope of the proposed framework can further be extended to include other effects that are defined in terms of displacement (for example, fringing capacitance of the MEMS actuator [19]). This work should aid in the study of ferroelectric negative capacitance for electrostatic MEMS applications.

ACKNOWLEDGMENTS

AA acknowledges support from SERB (Science and Engineering Research Board, Government of India) through SRG/2019/001229.

REFERENCES

- [1] V. Choudhary and K. Iniewski, *MEMS: Fundamental Technology and Applications*. CRC Press, 2016.
- [2] M. Gad-el Hak, *MEMS: Applications*. CRC press, 2005.
- [3] G. M. Rebeiz, *RF MEMS: Theory, Design, and Technology*. John Wiley & Sons, 2004.
- [4] C. Pawashe, K. Lin, and K. J. Kuhn, "Scaling limits of electrostatic nanorelays," *IEEE Trans. Electron Devices*, vol. 60, no. 9, pp. 2936–2942, 2013, doi:10.1109/TED.2013.2273217.
- [5] M. Masduzzaman and M. A. Alam, "Effective nanometer airgap of NEMS devices using negative capacitance of ferroelectric materials," *Nano Lett.*, vol. 14, no. 6, pp. 3160–3165, May. 2014, doi:10.1021/nl5004416.
- [6] S. Salahuddin and S. Datta, "Use of negative capacitance to provide voltage amplification for low power nanoscale devices," *Nano Lett.*, vol. 8, no. 2, pp. 405–410, Feb. 2008, doi:10.1021/nl071804g.
- [7] M. Kobayashi, "A perspective on steep-subthreshold-slope negative-capacitance field-effect transistor," *Appl. Phys. Express*, vol. 11, no. 11, p. 110101, 2018, doi:10.7567/APEX.11.110101.
- [8] L. Tu, X. Wang, J. Wang, X. Meng, and J. Chu, "Ferroelectric negative capacitance field effect transistor," *Adv. Electron. Mater.*, vol. 4, no. 11, p. 1800231, 2018, doi:10.1002/aeml.201800231.

- [9] A. I. Khan, K. Chatterjee, B. Wang, S. Drapcho, L. You, C. Serrao, S. R. Bakaul, R. Ramesh, and S. Salahuddin, "Negative capacitance in a ferroelectric capacitor," *Nature Mater.*, vol. 14, no. 2, pp. 182–186, Feb. 2015, doi:10.1038/nmat4148.
- [10] M. Hoffmann, F. P. Fengler, M. Herzig, T. Mittmann, B. Max, U. Schroeder, R. Negrea, P. Lucian, S. Slesazek, and T. Mikolajick, "Unveiling the double-well energy landscape in a ferroelectric layer," *Nature*, vol. 565, no. 7740, pp. 464–467, 2019, doi:10.1038/s41586-018-0854-z.
- [11] A. Islam Khan, D. Bhowmik, P. Yu, S. Joo Kim, X. Pan, R. Ramesh, and S. Salahuddin, "Experimental evidence of ferroelectric negative capacitance in nanoscale heterostructures," *Appl. Phys. Lett.*, vol. 99, no. 11, p. 113501, 2011, doi:10.1063/1.3634072.
- [12] N. Tasneem, P. V. Ravindran, Z. Wang, J. Gomez, J. Hur, S. Yu, S. Datta, and A. I. Khan, "Differential charge boost in hysteretic ferroelectric-dielectric heterostructure capacitors at steady state," *Appl. Phys. Lett.*, vol. 118, no. 12, p. 122901, 2021, doi:10.1063/5.0035880.
- [13] M. I. Younis, *MEMS Linear and Nonlinear Statics and Dynamics*. Boston, MA: Springer US, 2011, vol. 20.
- [14] K. Choe and C. Shin, "Adjusting the operating voltage of a nanoelectromechanical relay using negative capacitance," *IEEE Trans. Electron Devices*, vol. 64, no. 12, pp. 5270–5273, Dec. 2017, doi:10.1109/TED.2017.2756676.
- [15] R. Tattamangalam Raman, A. Ajoy, and R. Padmanabhan, "Analysis of electrostatic MEMS using energy-charge landscape," *IEEE Trans. Electron Devices*, vol. 67, no. 10, pp. 4413–4420, Oct. 2020, doi:10.1109/TED.2020.3018700.
- [16] P. Decuzzi, G. Demelio, G. Pascasio, and V. Zaza, "Bouncing dynamics of resistive microswitches with an adhesive tip," *J. Appl. Phys.*, vol. 100, no. 2, p. 024313, Jul. 2006, doi:10.1063/1.2214348.
- [17] A. Granaldi and P. Decuzzi, "The dynamic response of resistive microswitches: switching time and bouncing," *J. Micromech. Microeng.*, vol. 16, no. 7, p. 1108, Apr. 2006, doi:10.1088/0960-1317/16/7/002.
- [18] S. Chakraborty, A. Bhattacharya, and T. Bhattacharyya, "Experimental analysis of pull-out voltage of electrostatically actuated microcantilever beam based on contact-stiction model," *Micro & Nano Lett.*, vol. 6, no. 1, pp. 43–47, Jan. 2011, doi:10.1049/mnl.2010.0125.
- [19] Y. Nemirovsky and O. Bochobza-Degani, "A methodology and model for the pull-in parameters of electrostatic actuators," *J. Microelectromech. Syst.*, vol. 10, no. 4, pp. 601–615, Dec. 2001, doi:10.1109/84.967384.
- [20] R. Tattamangalam Raman and A. Ajoy, "SPICE-based multi-physics model to analyze the dynamics of ferroelectric negative-capacitance–electrostatic MEMS hybrid actuators," *IEEE Trans. Electron Devices*, vol. 67, no. 11, pp. 5174–5181, Nov. 2020, doi:10.1109/TED.2020.3019991.
- [21] S. Shekhar, K. Vinoy, and G. Ananthasuresh, "Surface-micromachined capacitive RF switches with low actuation voltage and steady contact," *J. Microelectromech. Syst.*, vol. 26, no. 3, pp. 643–652, 2017, doi:10.1109/JMEMS.2017.2688519.
- [22] M. Kobayashi and T. Hiramoto, "On device design for steep-slope negative-capacitance field-effect-transistor operating at sub-0.2 V supply voltage with ferroelectric HfO₂ thin film," *AIP Advances*, vol. 6, no. 2, p. 025113, 2016, doi:10.1063/1.4942427.
- [23] J. Iannacci, A. Repchankova, D. Macii, and M. Niessner, "A measurement procedure of technology-related model parameters for enhanced RF-MEMS design," in *2009 IEEE Int. Workshop on Advanced Methods for Uncertainty Estimation in Measurement*. IEEE, Jul. 2009, pp. 44–49, doi:10.1109/AMUEM.2009.5207609.
- [24] F. Giacomzzi and J. Iannacci, "RF MEMS technology for next-generation wireless communications," in *Handbook of Mems for Wireless and Mobile Applications*. Elsevier, 2013, pp. 225–257, doi:10.1533/9780857098610.1.225.
- [25] J. Oberhammer and G. Stemme, "Accuracy of quasi-static simulation methods as compared to full-dynamic analysis of nonlinear electrostatic MEMS actuators," in *2007 IEEE 20th Int. Conf. MEMS*. IEEE, 2007, pp. 187–190, doi:10.1109/MEMSYS.2007.4432961.
- [26] G. N. Nielson and G. Barbastathis, "Dynamic pull-in of parallel-plate and torsional electrostatic MEMS actuators," *J. Microelectromech. Syst.*, vol. 15, no. 4, pp. 811–821, 2006, doi:10.1109/JMEMS.2006.879121.
- [27] A. Saeidi, T. Rosca, E. Memisevic, I. Stolichnov, M. Cavaliere, L.-E. Wernersson, and A. M. Ionescu, "Nanowire tunnel FET with simultaneously reduced subthermionic subthreshold swing and off-current due to negative capacitance and voltage pinning effects," *Nano Lett.*, vol. 20, no. 5, pp. 3255–3262, 2020, doi:10.1021/acs.nanolett.9b05356.
- [28] A. Saeidi, F. Jazaeri, I. Stolichnov, G. V. Luong, Q.-T. Zhao, S. Mantl, and A. M. Ionescu, "Effect of hysteretic and non-hysteretic negative capacitance on tunnel FETs DC performance," *Nanotechnol.*, vol. 29, no. 9, p. 095202, 2018, doi:10.1088/1361-6528/aaa590.
- [29] A. I. Khan, M. Hoffmann, K. Chatterjee, Z. Lu, R. Xu, C. Serrao, S. Smith, L. W. Martin, C. Hu, R. Ramesh *et al.*, "Differential voltage amplification from ferroelectric negative capacitance," *Appl. Phys. Lett.*, vol. 111, no. 25, p. 253501, 2017, doi:10.1063/1.5006958.
- [30] A. I. Khan, K. Chatterjee, J. P. Duarte, Z. Lu, A. Sachid, S. Khandelwal, R. Ramesh, C. Hu, and S. Salahuddin, "Negative capacitance in short-channel FinFETs externally connected to an epitaxial ferroelectric capacitor," *IEEE Electron Device Lett.*, vol. 37, no. 1, pp. 111–114, 2015, doi:10.1109/LED.2015.2501319.
- [31] H. Choi and C. Shin, "Negative capacitance transistor with two-dimensional channel material (Molybdenum disulfide, MoS₂)," *physica status solidi (a)*, vol. 216, no. 16, p. 1900177, 2019, doi:10.1002/pssa.201900177.
- [32] E. Ko, J. W. Lee, and C. Shin, "Negative capacitance FinFET with sub-20-mV/decade subthreshold slope and minimal hysteresis of 0.48 V," *IEEE Electron Device Lett.*, vol. 38, no. 4, pp. 418–421, 2017, doi:10.1109/LED.2017.2672967.
- [33] J. Jo and C. Shin, "Negative capacitance field effect transistor with hysteresis-free sub-60-mV/decade switching," *IEEE Electron Device Lett.*, vol. 37, no. 3, pp. 245–248, 2016, doi:10.1109/LED.2016.2523681.
- [34] Y. Li, Y. Lian, and G. S. Samudra, "Quantitative analysis and prediction of experimental observations on quasi-static hysteretic metal-ferroelectric-metal-insulator-semiconductor FET and its dynamic behaviour based on Landau theory," *Semiconductor Science and Technology*, vol. 30, no. 4, p. 045011, 2015, doi:10.1088/0268-1242/30/4/045011.
- [35] Y. Li, "Negative capacitance ferroelectric MOSFET for low power circuits: Potential and limitations," Ph.D. dissertation, National University of Singapore, 2017. [Online]. Available: <https://scholarbank.nus.edu.sg/handle/10635/136521>
- [36] X. Wang, Y. Chen, G. Wu, D. Li, L. Tu, S. Sun, H. Shen, T. Lin, Y. Xiao, M. Tang *et al.*, "Two-dimensional negative capacitance transistor with polyvinylidene fluoride-based ferroelectric polymer gating," *NPJ 2D Mater. and Appl.*, vol. 1, no. 1, pp. 1–7, 2017, doi:10.1038/s41699-017-0040-4.
- [37] M. Si, C.-J. Su, C. Jiang, N. J. Conrad, H. Zhou, K. D. Maize, G. Qiu, C.-T. Wu, A. Shakouri, M. A. Alam, and P. D. Ye, "Steep-slope hysteresis-free negative capacitance MoS₂ transistors," *Nature Nanotechnol.*, vol. 13, no. 1, pp. 24–28, 2018, doi:10.1038/s41565-017-0010-1.
- [38] M. Hoffmann, B. Max, T. Mittmann, U. Schroeder, S. Slesazek, and T. Mikolajick, "Demonstration of high-speed hysteresis-free negative capacitance in ferroelectric Hf_{0.5}Zr_{0.5}O₂," in *2018 IEEE IEDM*. IEEE, 2018, pp. 31–6, doi:10.1109/IEDM.2018.8614677.
- [39] M. Kobayashi, N. Ueyama, K. Jang, and T. Hiramoto, "Experimental study on polarization-limited operation speed of negative capacitance FET with ferroelectric HfO₂," in *2016 IEEE IEDM*. IEEE, 2016, pp. 12–3, doi:10.1109/IEDM.2016.7838402.
- [40] T. Mikolajick, S. Slesazek, H. Mulaosmanovic, M. Park, S. Fichtner, P. Lomenzo, M. Hoffmann, and U. Schroeder, "Next generation ferroelectric materials for semiconductor process integration and their applications," *J. Appl. Phys.*, vol. 129, no. 10, p. 100901, 2021, doi:10.1063/5.0037617.
- [41] H. Ku and C. Shin, "Transient response of negative capacitance in P(VDF_{0.75}-TrFE_{0.25}) organic ferroelectric capacitor," *IEEE J. Electron Devices Soc.*, vol. 5, no. 3, pp. 232–236, 2017, doi:10.1109/JEDS.2017.2670546.
- [42] G. A. Salvatore, A. Rusu, and A. M. Ionescu, "Experimental confirmation of temperature dependent negative capacitance in ferroelectric field effect transistor," *Appl. Phys. Lett.*, vol. 100, no. 16, p. 163504, 2012, doi:10.1063/1.4704179.
- [43] F. W. DelRio, M. P. de Boer, J. A. Knapp, E. David Reedy, P. J. Clews, and M. L. Dunn, "The role of van der Waals forces in adhesion of micromachined surfaces," *Nature Mater.*, vol. 4, no. 8, pp. 629–634, 2005, doi:10.1038/nmat1431.
- [44] A. Hariri, J. Zu, and R. B. Mrad, "Modeling of dry stiction in micro electro-mechanical systems (MEMS)," *J. Micromech. Microeng.*, vol. 16, no. 7, p. 1195, May. 2006, doi:10.1088/0960-1317/16/7/012.
- [45] N. Tas, T. Sonnenberg, H. Jansen, R. Legtenberg, and M. Elwenspoek, "Stiction in surface micromachining," *J. Micromech. Microeng.*, vol. 6, no. 4, p. 385, 1996, doi:10.1088/0960-1317/6/4/005.
- [46] K. Choe and C. Shin, "Ferroelectric-gated nanoelectromechanical non-volatile memory cell," *IEEE Trans. Electron Devices*, vol. 66, no. 1, pp. 407–412, Jan. 2019, doi:10.1109/TED.2018.2881201.